Document Version
Final published version

Citation (APA)
Xiong, X., R. Negenborn, R., & Pang, Y. (2026). Model predictive formation control of multi-vessel systems considering ship-to-ship interaction. *Journal of Marine Science and Technology*. https://doi.org/10.1007/s00773-026-01111-4

Journal of Marine Science and Technology
https://doi.org/10.1007/s00773-026-01111-4

ORIGINAL ARTICLE

Model predictive formation control of multi-vessel systems considering ship-to-ship interaction

Xin Xiong[1] · **Rudy R. Negenborn**[1] · **Yusong Pang**[1]

Received: 23 June 2025 / Accepted: 11 February 2026

Abstract

The formation control of autonomous surface vessels presents significant challenges when operating in close proximity, where ship-to-ship interaction becomes non-negligible. While conventional formation control methods often neglect these interactions or simplify them excessively, this paper develops a centralized model predictive control (MPC) framework that explicitly incorporates a three-degrees-of-freedom interaction model. This interaction model is constructed empirically based on existing computational fluid dynamics results, offering an efficient and practical way to approximate proximity-induced forces in real-time. The proposed control strategy enables accurate trajectory tracking and effective disturbance adaptation in typical formation geometries, including platooning, parallel, and triangular formations. Simulation results demonstrate that the MPC controller can outperform traditional PID controllers in both tracking precision and interaction robustness across the configurations. Formation-specific performance differences are also analyzed in detail.

Keywords Multi-vessel systems · Model predictive control · Ship-to-ship interaction · Formation control

1 Introduction

Autonomous surface vessels (ASVs), as an emerging technology in the maritime domain, have attracted significant academic and industrial interest in their potential to transform waterborne transportation and operations. Their applications span diverse fields, such as remote sensing, maritime surveillance, oceanographic research, offshore energy exploration [1–4]. Compared to conventional vessels, autonomous ships provide greater operational efficiency, enhanced safety, and potential for greener navigation [5]. Compared to a single ASV, cooperation among multiple ASVs can improve the safety, efficiency, and resource utilization of waterborne transport, thus optimizing overall transport performance [6]. Nevertheless, as the fleet size grows, effective coordination becomes increasingly difficult—especially under cooperative control approaches designed to meet multiple objectives across multiple ASVs.

In cooperative control, formation control is frequently discussed with the goal of guiding a group of vessels to achieve a specific geometric configuration while navigating along a desired path. Three geometric configurations are typically considered: platooning, parallel, and triangular formation [7–9]. Numerous methods have been proposed to achieve these arrangements, including the leader-follower method [10–12], behavioral methods [13], and virtual structure methods [14]. These control strategies not only ensure the overall stability and coherence of the formation but also provide a structural foundation for addressing issues such as obstacle avoidance, path planning, and task allocation during formation sailing.

Designing robust formation motion controllers is inherently challenging due to the nonlinear of the ASV system and underactuated characteristics, as well as physical constraints such as the actuator saturation and path adherence. To address these challenges, a variety of control schemes have been proposed, including sliding-mode control [15], adaptive and neural-network-based approaches [16], and virtual trajectory-based predictive control [17]. Among these, model predictive control (MPC) has received particular attention for its ability to handle multi-input multi-output systems under complex constraints while providing real-time optimization.

✉ Yusong Pang
Y.Pang@tudelft.nl

Xin Xiong
X.Xiong-1@tudelft.nl

Rudy R. Negenborn
R.R.Negenborn@tudelft.nl

[1] Maritime and Transport Technology, Delft University of Technology, Delft, The Netherlands

Its predictive capability and flexibility make it especially suitable for ASVs formation control, where physical limitations, safety margins, and trajectory tracking must be jointly managed. As a result, MPC has become one of the most widely adopted frameworks in recent ASV control research [18–22].

However, a critical factor often overlooked in the literature is the ship-to-ship interaction, which arises when multiple vessels operate in close proximity. In some practical formation scenarios, the relative distances between vessels are frequently smaller than twice the vessel length, making the resulting hydrodynamic interaction forces non-negligible. These interaction effects can induce significant surge, sway, and yaw disturbances, potentially undermining the effectiveness of conventional controllers that do not account for them [23]. While several studies have reported the influence of hydrodynamic interactions on vessel behavior through CFD or experimental analysis, few have proposed dynamic models that can be systematically applied within a real-time control framework.

While previous studies—including our earlier work [24] —have started to investigate these effects in basic two-ship platooning setups, there remains a lack of generalized models and formation-wide control strategies that incorporate multi-axis ship-to-ship interaction.

This study aims to address this gap by developing a centralized MPC framework that explicitly considers ship-to-ship interaction. An empirical three-degree-of-freedom interaction model is constructed using trends extracted from existing CFD data, allowing efficient approximation of nonlinear hydrodynamic effects without relying on first-principles formulations. To improve control performance, the proposed controller incorporates a coordinate transformation that decouples yaw-induced sway dynamics, thereby enhancing lateral stability and tracking smoothness, particularly in curved trajectories. The effectiveness and adaptability of the framework are demonstrated through systematic validation across three typical formation configurations—platooning, parallel, and triangular—each exhibiting distinct interaction characteristics. The results highlight the practicality of the proposed approach in capturing key dynamic effects and ensuring robust formation control under proximity-induced disturbances.

In summary, the present paper extends the previous study in four aspects: (i) we generalise to a three-vessel formation and consider three representative geometries (platooning, parallel and triangular) that exhibit distinct interaction patterns; (ii) we employ a reproducible 3-DOF ship-to-ship interaction formulation with coefficient sets identified from CFD-referenced data (Sect. 2.2 and Tables 5, 6 and 7); (iii) we upgrade the control layer from PID to a constrained MPC formulation that explicitly handles actuator limits and penalises control increments; and (iv) we integrate a coordinate transformation to enable consistent tracking and spacing regulation across straight and curved manoeuvres.

The vessel motion considered in this paper is described by a standard nonlinear 3-DOF maneuvering model, which already captures the internal hydrodynamic nonlinearities of each ship. The ship-to-ship interaction terms introduced in Sect. 2 enter the dynamics as additional, geometry-dependent forces and moment that depend on the relative position and speed of neighboring vessels. From a control viewpoint, these interactions therefore act as structured, state-dependent disturbances on top of the nominal nonlinear ship model, rather than as a reparameterization of its internal dynamics. Various nonlinear control techniques—such as back-stepping, sliding-mode and adaptive controllers—could in principle be designed to cope with internal model uncertainties and nonlinearities. A systematic benchmark between such controllers and the proposed interaction-aware MPC, however, would require a dedicated study, including careful tuning and constraint handling for each method, and would go beyond the scope of this paper. Here, the emphasis is on demonstrating how a physically motivated interaction model and the coordinate transformation introduced in Sect. 3 can be embedded into a constrained MPC framework, and how this combined design improves lateral stability and tracking performance in different formation geometries.

The remainder of this paper is organized as follows. Section 2 presents the modeling framework, including the empirical ship-to-ship interaction model and the kinematic and dynamic formulations of the multi-vessel system. Section 3 details the design of the proposed model predictive control scheme. Section 4 conducts numerical simulations across three representative formation configurations to evaluate the control strategy under realistic interaction effects. Finally, Sect. 5 summarizes the main findings and outlines potential directions for future research.

2 Formation system modeling

To investigate the impact of ship-to-ship interaction in formation control, we consider a three-vessel formation system, which serves as the minimal configuration to simultaneously capture both pairwise hydrodynamic couplings and geometric complexity beyond simple leader–follower structures. Compared to two-ship setups, which typically focus only on surge-direction effects in platooning formations [24, 25], a three-vessel arrangement enables the study of interaction-induced disturbances in surge, sway, and yaw directions across multiple formation geometries (e.g., parallel and triangular).

Moreover, this setup facilitates generalization to larger fleets by preserving interaction structure and control topology, as additional vessels can be incorporated in a modular

Fig. 1 The geometric configuration of formation

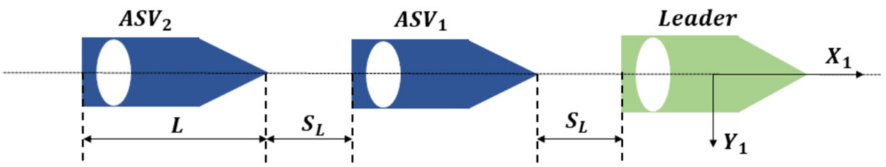

a The platooning formation

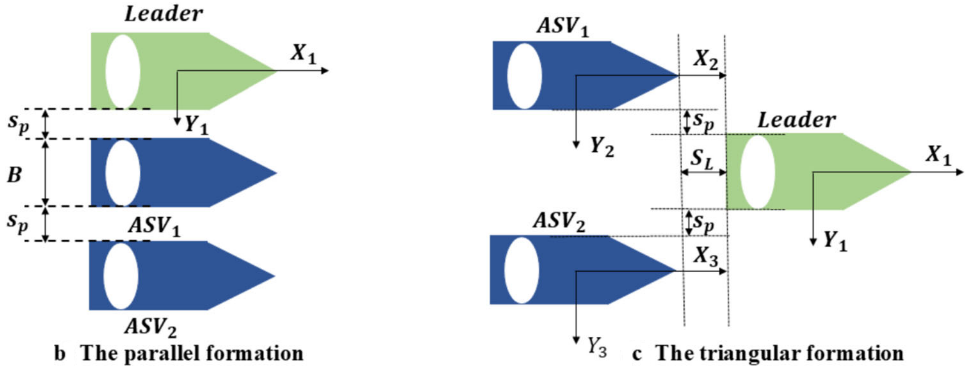

b The parallel formation

c The triangular formation

manner. Similar modeling approaches have been used in cooperative ASV control and hydrodynamic simulation studies [26, 27], where three-vessel configurations provide a balanced trade-off between complexity and interpretability. Thus, the proposed model and control design are scalable and can be extended to multi-vessel systems beyond three ships.

As depicted in Fig. 1, each formation configuration—platooning, parallel, and triangular–plays a role in shaping ship-to-ship interaction. In all three configurations, the green vessel serves as the leader, while the blue vessels act as followers. The origin of the body-fixed coordinate system is in the center of the ship, with the X, Y, and Z axes pointing to the forward, starboard, and downward, respectively. In platooning formation (as shown in Fig. 1a), the longitudinal distance between the two ships is indicated by S_L, without transverse offset. In parallel formation (as shown in Fig. 1b), the bows of the hull are aligned and the transverse separations are S_p without any longitudinal offset. The layout of the triangular formation is shown in Fig. 1c, where L and B represent the length and width of the ship, respectively.

2.1 Ship dynamics

The formation system consists of a group of three ASVs, with each vessel modeled in both an earth-fixed inertial reference frame and a body-fixed reference frame. Each vessel is assumed to have a plane of symmetry and the heave, pitch, and roll motions are ignored. The kinematics and dynamics model [28] of the ASV_i are described as follows:

$$\begin{cases} \dot{\eta}_i = R_i(\psi_i)\nu_i \\ M_i\dot{\nu}_i = -C_i(\nu_i)\nu_i - D_i(\nu_i)\nu_i - g_i(\nu_i, \eta_i) \\ \qquad + \tau_{is}(\nu_i, \eta_i) + \tau_i, \end{cases} \tag{1}$$

where $\eta_i = \left[x_i\ y_i\ \psi_i\right]^T$ is the vector denoting the ship position (x_i, y_i) and heading ψ_i with coordinates in the earth-fixed frame; $\nu_i = \left[u_i\ v_i\ r_i\right]^T$ is the vector denoting the ship velocities in the body-fixed frame containing the velocity of surge u_i, sway v_i, and yaw r_i; $g_i(\eta_i, \nu_i) \in \mathbb{R}^3$ denotes the unmodeled hydrodynamics. The control input vector is $\tau_i = \left[\tau_{iu}\ \tau_{iv}\ \tau_{ir}\right]^T \in \mathbb{R}^3$. The terms $M_i \in \mathbb{R}^{3\times3}$, $C_i \in \mathbb{R}^{3\times3}$, and $D_i \in \mathbb{R}^{3\times3}$ are the mass (inertia), Coriolis-centripetal, and damping matrix, respectively. $\tau_{is} = [\tau_{isu}, \tau_{isv}, \tau_{isr}]^T \in \mathbb{R}^3$ is the ship-to-ship interaction forces and moments. $R_i(\psi_i) \in \mathbb{R}^{3\times3}$ denotes a rotation matrix. These matrices are given below:

$$M_i = \begin{bmatrix} m_{11i} & 0 & 0 \\ 0 & m_{22i} & m_{23i} \\ 0 & m_{23i} & m_{33i} \end{bmatrix},$$
$$D_i(\nu_i) = -\begin{bmatrix} d_{11i}(u_i) & 0 & 0 \\ 0 & d_{22i}(\nu_i, r_i) & d_{23i}(\nu_i, r_i) \\ 0 & d_{32i}(\nu_i, r_i) & d_{33i}(\nu_i, r_i) \end{bmatrix},$$
$$C_i(\nu_i) = \begin{bmatrix} 0 & 0 & -m_{22i}v_i - m_{23i}r_i \\ 0 & 0 & m_{11i}u_i \\ m_{22i}v_i + m_{23i}r_i & -m_{11i}u_i & 0 \end{bmatrix},$$
$$R_i(\psi_i) = \begin{bmatrix} \cos(\psi_i) & -\sin(\psi_i) & 0 \\ \sin(\psi_i) & \cos(\psi_i) & 0 \\ 0 & 0 & 1 \end{bmatrix}. \tag{2}$$

2.2 Model of ship-to-ship interaction

Hydrodynamic interactions between ships in formation are influenced by factors such as ship geometry, navigation speed, inter-ship distance, water depth, and environmental conditions. In this paper, the ships are homogeneous ASVs, with the focus mainly on speed and inter-ship distance. When the longitudinal distance between two ships exceeds twice the length of the vessel, the hydrodynamic effects nearly vanish [29]. Consequently, this study addresses ship-to-ship interaction primarily at shorter distances—specifically, when the longitudinal gap is under twice the vessel's length and the lateral gap is under twice its width.

Ship-to-ship interaction generally arise when vessels operate in close proximity, causing hydrodynamic forces that can lead to attraction or repulsion. Many studies have investigated these interactions across various scenarios, such as head-on encounters and overtaking [25, 30, 31], parallel movements during replenishment or lightering operations [32–34], and when ships in formation move in different configurations [26, 27]. These findings highlight how hydrodynamic effects can significantly alter a vessel's motion during ship-to-ship interaction, underscoring the importance of factoring in these forces during formation control. However, most of these studies focus on empirical observation or CFD analysis of individual cases, and few provide a unified or dynamic interaction force model that can be directly integrated into control system design for real-time applications.

In previous work [24], ship-to-ship interaction forces were approximated using simplified expressions that only considered surge dynamics in a two-vessel platooning configuration. However, practical formations involve interactions in all three motion axes—surge, sway, and yaw—which can affect vessel stability and tracking. Accurately modeling these effects remains challenging due to the nonlinear and geometry-dependent nature of hydrodynamic coupling.

To capture these effects without resorting to computationally intensive CFD simulations, we adopt a data-informed, black-box interaction model. The model is empirically derived based on relative position and velocity terms and structured to reflect dominant nonlinear trends observed in prior CFD studies on ship-to-ship interaction [27, 29, 30]. These studies indicate that surge interaction forces typically grow approximately cubically with speed, while sway forces exhibit predominantly quadratic dependence on the lateral velocity, with yaw moments coupling both surge and sway motions. Although the proposed model does not provide a first-principles physical derivation, it serves as an effective model for estimating proximity-induced forces in real time.

In this study, environmental disturbances such as wind, waves and current are deliberately excluded from the modelling framework. From a mathematical viewpoint, the interaction forces in (1) enter the dynamics as external disturbances and could in principle be superimposed with environmental loads. However, environmental effects are typically unstructured, stochastic and slowly varying at the time scales considered here, whereas ship-to-ship interaction are strongly geometry-dependent and change rapidly with the relative motion of neighboring vessels. Including both effects simultaneously would make it difficult to disentangle their respective impact on the formation behavior and to assess the specific contribution of the interaction model. Therefore, in this first study we focus on the structured, geometry-dependent disturbance component due to ship-to-ship hydrodynamics, and leave the combination with stochastic environmental disturbances to future work.

Specifically, for the ASV_i when next to the ASV_j, the ship-to-ship interaction forces and moments $\tau_{is} = [\tau_{isu}, \tau_{isv}, \tau_{isr}]^T$ are modeled as:

$$\begin{cases} \tau_{isu} = \alpha_{11}u^3 + \big(\alpha_{12}(x_i - x_j) + \alpha_{13}(y_i - y_j)\big)\, u^2 + \epsilon_1 \\ \tau_{isv} = \alpha_{21}u^3 + \big(\alpha_{22}(x_i - x_j) + \alpha_{23}(y_i - y_j)\big)\, v^2 + \epsilon_2 \\ \tau_{isr} = \alpha_{31}u^3 r + \big(\alpha_{32}(x_i - x_j) + \alpha_{33}(y_i - y_j)\big)\, v^2 r + \epsilon_3, \end{cases} \tag{3}$$

where the coefficient matrix $\boldsymbol{\alpha} = [\alpha_{mn}] \in \mathbb{R}^{3\times 3}$ collects scalar hydrodynamic coefficients $\alpha_{mn} \in \mathbb{R}$ identified from CFD-referenced interaction-force datasets over the relative-position and relative-velocity ranges considered in this paper [27]; the resulting coefficient sets for the three scenarios are reported in Tables 5, 6 and 7. For multi-vessel formations, the net interaction load on vessel i is computed by pairwise superposition, $\boldsymbol{\tau}_{is,i} = \sum_{j\neq i} \boldsymbol{\tau}_{i\leftarrow j}$. No symmetry is enforced a priori, i.e., $\boldsymbol{\tau}_{i\leftarrow j} \neq -\boldsymbol{\tau}_{j\leftarrow i}$ in general, since the upstream flow environment is direction-dependent in close-spacing operations. The modelling-error term $\boldsymbol{\varepsilon}$ is treated as a bounded disturbance satisfying $\|\boldsymbol{\varepsilon}\| \leq \bar{\varepsilon}$, where $\bar{\varepsilon}$ is chosen based on the worst-case identification residual.

3 Controller design

The formation control of multi-vessel systems presents significant challenges due to the presence of multiple control inputs, nonlinear dynamics, physical constraints, and some external disturbances [35]. The complexity is further exacerbated by ship-to-ship interaction, which introduce nonlinear and coupled hydrodynamic forces when vessels operate in close proximity.

Model predictive control (MPC) has emerged as a powerful framework for addressing such challenges, owing to its capability to handle multi-input multi-output systems with constraints while optimizing control performance in real time. MPC also exhibits strong robustness to dynamic variations and bounded uncertainties, making it particularly well-suited for autonomous surface vessel (ASV) formation scenarios involving interaction effects.

The overall control architecture is illustrated in Fig. 2. The upper layer generates the desired trajectory and reference speed for each ASV based on high-level formation objectives. These references are then provided to a lower-level MPC controller, which computes the optimal control inputs

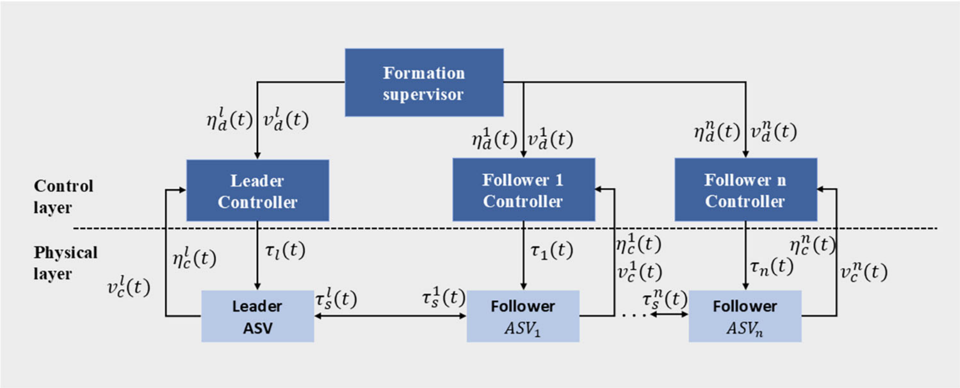

Fig. 2 Formation control scheme

by considering both the vessel's real-time state and the estimated ship-to-ship interaction forces.

To enhance control performance and facilitate the design of the model predictive controller, the ASV motion dynamics are reformulated into a more structured form by separating kinematics and dynamics. The original system dynamics contain coupling terms such as the yaw moment τ_{ir} directly affecting sway motion due to the off-diagonal inertia term m_{23i}. These couplings make direct controller design challenging.

To address this, we introduce a coordinate transformation that eliminates the direct coupling between yaw and sway by shifting the sway velocity state to a transformed state variable [36]:

$$\bar{v}_i = v_i + \delta_i r_i, \quad \text{where } \delta_i = \frac{m_{23i}}{m_{22i}}. \tag{4}$$

In addition, we define a new auxiliary vector $\boldsymbol{\phi}_i = [\phi_{ui}, \phi_{vi}, \phi_{ri}]^\top$, which captures the residual dynamics excluding the direct control input:

$$\boldsymbol{\phi}_i = M_i^{-1}\left(-C_i(v_i)v_i - D_i(v_i)v_i - g(v_i,\eta_i) + \tau_i^s\right), \tag{5}$$

where τ_i^s represents the ship-to-ship interaction forces. These terms can be viewed as a generalized "drift" vector summarizing the passive system response due to damping, Coriolis forces, and interaction.

After transformation, the full state-space dynamics of the ASV_i can be rewritten as:

$$\begin{aligned}
\dot{\bar{x}}_i &= u_i \cos\psi_i - \bar{v}_i \sin\psi_i, \\
\dot{\bar{y}}_i &= u_i \sin\psi_i + \bar{v}_i \cos\psi_i, \\
\dot{\psi}_i &= r_i, \\
\dot{u}_i &= \phi_{ui} + \frac{1}{m_{11i}}\tau_{iu}, \\
\dot{\bar{v}}_i &= \phi_{vi} + \frac{1}{m_{22i}}\tau_{iv} + \frac{m_{23i}}{m_{22i}}\phi_{ri}, \\
\dot{r}_i &= \phi_{ri} + \frac{1}{\Delta_i}\tau_{ir}, \quad \text{where } \Delta_i = m_{22i}m_{33i} - m_{23i}^2.
\end{aligned} \tag{6}$$

This transformation decouples certain dynamic terms, particularly in the sway–yaw interaction, and simplifies the formulation of predictive control. It ensures smoother lateral behavior under hydrodynamic disturbances and stabilizes lateral error evolution in formation tasks.

Define $X_i = \left[\bar{x}_i \ \bar{y}_i \ \psi_i \ u_i \ \bar{v}_i \ r_i\right]^T$ as the new system state variable and $U_i = \left[\tau_{iu} \ \tau_{iv} \ \tau_{ir}\right]^T$ as the control input. The state space model for $i-th$ ASV is given by:

$$\dot{X}_i = f(X_i, U_i) = \begin{cases} R_i(\psi_i)v_i \\ \boldsymbol{\phi}_i + M_i^{-1}U_i \end{cases}, \quad y_i = PX_i \tag{7}$$

where the function $f(\mathbb{R}^6 \times \mathbb{R}^2 \to \mathbb{R}^6)$ represents the nonlinear equations of the ASV motion model, P is defined as: $P = \begin{bmatrix} 1 & 0 & 0 & 0 & 0 & 0 \\ 0 & 1 & 0 & 0 & 0 & 0 \end{bmatrix}$ and $\boldsymbol{\phi}_i$ is as follow:

$$\begin{aligned}
\phi_{ui} &= \frac{m_{22i}}{m_{11i}}v_i r_i + \frac{m_{23i}}{m_{11i}}r_i^2 - \frac{d_{11i}(u_i)}{m_{11i}}u_i + \frac{\tau_{isu}}{m_{11i}}, \\
\phi_{vi} &= -\frac{m_{11i}}{m_{22i}}u_i r_i - \frac{d_{22i}(v_i, r_i)}{m_{22i}}v_i - \frac{d_{23i}(v_i, r_i)}{m_{22i}}r_i + \frac{\tau_{isv}}{m_{22i}}, \\
\phi ri &= \frac{m_{11i}m_{22i} - m_{23i}^2}{\Delta_i}u_i v_i + \frac{m_{11i}m_{23i} - m_{23i}m_{22i}}{\Delta_i}u_i r_i \\
&\quad - \frac{m_{22i}}{\Delta_i}\left(d_{33i}(v_i, r_i)r_i + d_{32i}(v_i, r_i)v_i\right) \\
&\quad + \frac{\Delta_i}{m_{23i}}\left(d_{23i}(v_i, r_i)r_i + d_{22i}(v_i, r_i)v_i\right) + \frac{\tau_{isr}}{m_{33i}}.
\end{aligned} \tag{8}$$

Assumption The $\boldsymbol{\phi}_i$ is invariant over a short period of time $[k, k+nT]$ [37]. This assumption is reasonable since only the first element of the optimal control input series computed is used, and the future control input series is recomputed at the next sampling time.

Let $\dot{X}_{iR} = f(X_{iR}, U_{iR})$ be the reference trajectory of $i-th$ ASV. Perform a first-order Taylor expansion of the function at the current reference point (X_{iR}, U_{iR}), and then an approximate discretization method, the Euler method, is used to discretize the motion state equation, with the sampling period denoted as T, as shown below:

$$\begin{cases} \tilde{X}_i(k+T) = A_{ik}\tilde{X}_i(k) + B_{ik}\tilde{U}_i(k) \\ \tilde{y}_i(k) = P\tilde{X}_i(k), \end{cases} \tag{9}$$

where $A_{ik} = I + T \cdot A_i$, $B_{ik} = T \cdot B_i$, $A_i = \left.\frac{\partial f}{\partial \mathbf{X}}\right|_{\mathbf{X_i}=\mathbf{X}_{iR},\, \mathbf{U_i}=\mathbf{U}_{iR}}$, and $B_i = \left.\frac{\partial f}{\partial \mathbf{U}}\right|_{\mathbf{X_i}=\mathbf{X}_{iR},\, \mathbf{U_i}=\mathbf{U}_{iR}}$, $\tilde{\mathbf{X}}_\mathbf{i} = \mathbf{X_i} - \mathbf{X}_{iR}$, $\tilde{\mathbf{U}}_\mathbf{i} = \mathbf{U_i} - \mathbf{U}_{iR}$.

The sampling time is set to $T = 1$ s, which is sufficiently small relative to the dominant manoeuvring time constants of the model, so that the one-step linearisation and Euler discretisation in (9) provide an adequate local approximation. In all simulation runs, the resulting QP was solved at every sampling instant using `quadprog`, and a feasible optimal solution was obtained without infeasibility or early termination.

In the actual process, there are actuator increment limitations, actuator saturation, and velocity constraints present in the system. Therefore, the state variables and control inputs of the system need to satisfy certain constraints, which are generally as follows:

$$\begin{cases} \Delta U_{i\,\min} \leq \Delta U_i(k+j) \leq \Delta U_{i\,\max}, \quad j = 0, 1, \ldots, N_c - 1 \\ U_{i\,\min} \leq U_i(k+j) \leq U_{i\,\max}, \quad j = 0, 1, \ldots, N_c - 1 \\ y_{i\,\min} \leq y_i(k+j) \leq y_{i\,\max}, \quad j = 0, 1, \ldots, N_p, \end{cases} \tag{10}$$

where N_p is the prediction horizon, N_c is the control horizon, $\Delta U_{i\,\min}$ and $\Delta U_{i\,\max}$ are the input increment constraints, $U_{i\,\min}$ and $U_{i\,\max}$ are the input constraints, $y_{i\,\min}$ and $y_{i\,\max}$ are the output constraints, and the condition $\Delta U_i(k+j) = U_i(k+j) - U_i(k+j-1)$ must be satisfied. It should be noted that $N_p \geq N_c$, and $U_i(k+j) = U_i(k+N_c-1), \quad J = N_c, \ldots, N_p-1$. To simultaneously handle the constraint conditions, the new state variable of the system $\xi_i(k)$ is defined as:

$$\begin{aligned} &\xi_i(k+1) = \tilde{A}_{ik}\xi(k) + \tilde{B}_{ik}\Delta U_i(k) \\ &\tilde{y}_i(k) = \tilde{C}_{ik}\xi(k), \end{aligned} \tag{11}$$

where $\tilde{\xi}_{ik} = \begin{bmatrix} \tilde{X}_i(k) \\ \tilde{U}_i(k-1) \end{bmatrix}$, $\tilde{A}_{ik} = \begin{bmatrix} A_{ik} & B_{ik} \\ \mathbf{0}_{m\times n} & I_m \end{bmatrix}$, $\tilde{B}_{ik} = \begin{bmatrix} B_{ik} \\ I_m \end{bmatrix}$, and $\tilde{C}_{ik} = \begin{bmatrix} P & \mathbf{0}_{2\times m} \end{bmatrix}$. Here, m is the dimension of the system control variables, and n is the dimension of the system state variables. For this ASV motion model, $m = 3$ and $n = 6$. For computational simplicity, within the prediction horizon N_p, it is assumed that:

$$A_{ik+j} = A_{ik}, \quad B_{ik+i} = B_{ik}, \quad j = 1, 2, \ldots, N_p \tag{12}$$

According to Eqs. 11 and 12, the predicted output of the system at time step k can be expressed as follows:

$$\tilde{Y}_i(k) = \Psi_{ik} + \Theta_{ik}\Delta\bar{U}_i(k), \tag{13}$$

where $\tilde{Y}_i(k)$ represents the predicted output within the prediction horizon N_p, $\Delta\bar{U}_i(k)$ denotes the predicted input within the control horizon N_c, and Ψ_{ik} and Θ_{ik} are system matrices. They are specifically defined as follows:

$$\tilde{Y}_i(k) = \begin{bmatrix} \tilde{y}_i(k+1) \\ \tilde{y}_i(k+2) \\ \vdots \\ \tilde{y}_i(k+N_c) \\ \vdots \\ \tilde{y}_i(k+N_p) \end{bmatrix}, \quad \Psi_k = \begin{bmatrix} \tilde{C}_{ik}\tilde{A}_{ik} \\ \tilde{C}_{ik}\tilde{A}_{ik}^2 \\ \vdots \\ \tilde{C}_{ik}\tilde{A}_{ik}^{N_c} \\ \vdots \\ \tilde{C}_{ik}\tilde{A}_{ik}^{N_p} \end{bmatrix},$$

$$\Delta\bar{U}_i(k) = \begin{bmatrix} \Delta\mathbf{U}_i(k) \\ \Delta\mathbf{U}_i(k+1) \\ \vdots \\ \Delta\mathbf{U}_i(k+N_c-1) \end{bmatrix},$$

$$\Theta_{ik} = \begin{bmatrix} \tilde{C}_{ik}\tilde{B}_{ik} & 0 & \cdots & 0 \\ \tilde{C}_{ik}\tilde{A}_{ik}\tilde{B}_{ik} & \tilde{C}_{ik}\tilde{B}_{ik} & \cdots & 0 \\ \vdots & \vdots & \ddots & \vdots \\ \tilde{C}_{ik}\tilde{A}_{ik}^{N_c-1}\tilde{B}_{ik} & \tilde{C}_{ik}\tilde{A}_{k}^{N_c-2}\tilde{B}_k & \cdots & \tilde{C}_k\tilde{B}_k \\ \tilde{C}_{ik}\tilde{A}_{ik}^{N_c}\tilde{B}_{ik} & \tilde{C}_{ik}\tilde{A}_{ik}^{N_c-1}\tilde{B}_{ik} & \cdots & \tilde{C}_{ik}\tilde{A}_{ik}\tilde{B}_{ik} \\ \vdots & \vdots & \ddots & \vdots \\ \tilde{C}_{ik}\tilde{A}_{ik}^{N_p-1}\tilde{B}_{ik} & \tilde{C}_{ik}\tilde{A}_{ik}^{N_p-2}\tilde{B}_{ik} & \cdots & \tilde{C}_{ik}\tilde{A}_{ik}^{N_p-N_c}\tilde{B}_{ik} \end{bmatrix}.$$

To enable the ASV to track the desired trajectory quickly and smoothly, the objective function is constructed based on deviations in the state variables of the system, control inputs, and control input increments. When designing the objective function, both the tracking accuracy and the energy efficiency of the system inputs should be considered. The objective function of $i-th$ is defined as follows:

$$J_i(k) = \sum_{j=1}^{N_p} \|\tilde{y}_i(k+j)\|_{Q_i}^2 + \sum_{j=0}^{N_c-1} \left\|\Delta\bar{U}_i(k+j)\right\|_{R_i}^2 \tag{14}$$

where Q_i and R_i are weight matrices, which can be adjusted according to different control requirements. Based on the above derivations, the optimization problem for $i-th$ ASV can be further reformulated as a quadratic programming form as follows:

$$\min_{\Delta\bar{U}_i(k)} J(\Delta\bar{U}_i(k)) = \frac{1}{2}\Delta\bar{U}_i(k)^T H_{ik}\Delta\bar{U}_i(k) + W_{ik}^T\Delta\bar{U}_i(k), \tag{15}$$

where

$$H_{ik} = 2\left(\Theta_{ik}^{T}\bar{Q}_i\Theta_{ik} + \bar{R}_i\right), \quad W_{ik} = 2\Theta_{ik}^{T}\bar{Q}_i\left[\boldsymbol{\Psi}_{ik}\xi_i(k)\right], \tag{16}$$

$$\bar{Q}_i = \begin{bmatrix} Q_i & \cdots & 0 \\ \vdots & \ddots & \vdots \\ 0 & \cdots & Q_i \end{bmatrix}_{N_p \times N_p}, \quad \bar{R}_i = \begin{bmatrix} R_i & \cdots & 0 \\ \vdots & \ddots & \vdots \\ 0 & \cdots & R_i \end{bmatrix}_{N_c \times N_c}. \tag{17}$$

Given the desired trajectory provided by the top layer, the centralized MPC-based trajectory tracking for the i-th ASV can be formulated as the following optimization problem:

$$\begin{aligned} &\underset{\Delta\bar{U}_i(k)}{\arg\min}\, J\left(\Delta\bar{U}_i(k)\right) \\ &s.t. \\ &\tilde{\mathbf{Y}}_i(k) = \boldsymbol{\Psi}_{ik}\boldsymbol{\xi}_i(k) + \Theta_{ik}\Delta\bar{U}_i(k), \\ &\Delta U_{i\,\min} \le \Delta U_i(k+j) \le \Delta U_{i\,\max}, \\ &U_{i\,\min} \le U_i(k+j) \le U_{i\,\max}, \\ &y_{i\,\min} \le y_i(k+j) \le y_{i\,\max}. \end{aligned} \tag{18}$$

Overall, the MPC-based centralized control scheme for a multi-ASV system considering ship-to-ship interaction to perform trajectory tracking is summarized in the following Algorithm 1.

Remark on prediction model vs. simulation plant. The MPC optimisation relies on the linearised and Euler-discretised prediction model in (9)–(18) to formulate a convex QP at each sampling instant, whereas the closed loop results in Sect. 4 are obtained by integrating the original nonlinear 3-DOF dynamics. Therefore, the evaluation already involves a model mismatch between the internal MPC prediction model and the nonlinear plant, rather than a fully "same-model" design–test setup.

Although a rigorous Lyapunov-based proof is beyond the scope of this paper, the proposed MPC formulation follows the standard structure of stabilizing tracking MPC schemes for nonlinear systems. The continuous-time ship dynamics are linearized around the time-varying reference trajectory and discretised with a sufficiently small sampling period, leading to a linear time-varying error system with bounded perturbations due to ship-to-ship interaction and unmodeled hydrodynamics. The quadratic cost penalizes tracking errors and control increments, while actuator and state constraints are explicitly enforced through the quadratic programmer in (14)– (17). With a positive semi-definite state weighting matrix $\boldsymbol{Q}_i \succeq 0$ and a positive definite control weighting matrix $\boldsymbol{R}_i \succ 0$, this programmer is strictly convex and admits a unique minimizer at each sampling instant. In combination with the receding-horizon strategy, this yields practical closed-loop stability in the sense that the tracking error remains bounded and converges to a small neighborhood of the reference trajectory, whose size depends on the magnitude of the interaction forces and other disturbances. This behavior is consistent with the simulation results in Sect. 4, where position and velocity errors remain small for all three formation configurations.

4 Simulation experiments

In formation control, the initial task is to generate the formation. There are three common formation configurations, illustrated in Fig. 1. This section conducts formation control simulations for these three configurations using the same desired trajectory to verify the effectiveness of the proposed control strategy. The simulation results will be analyzed and discussed.

The three ASVs are modeled based on the TitoNeri, the ASV has length $L = 0.97\,\text{m}$ and beam $B = 0.3\,\text{m}$ (see [38] and the RAS documentation). The longitudinal and lateral formation spacings are therefore reported also in nondimensional form as $\bar{S}_L = S_L/L, \bar{S}_p = S_p/B$. In the considered scenarios, $\bar{S}_L \in [0.3, 2.5]$ and $\bar{S}_p \in [0.5, 4]$, which correspond to close-spacing regimes where ship-to-ship interaction are expected to be relatively large. The other parameters of the hydrodynamic model of TitoNeri are shown in Table 1. The model of TitoNeri replaces the whole damping part D(vt)v(t) to the drag forces vector $\tau_{\text{drag}}(t)$ shown as follow:

$$\tau_{\text{drag}}(t) = \begin{bmatrix} \tau_{\text{drag}/u}(\varphi(t)) \cdot u(t) \\ \tau_{\text{drag}/v}(\varphi(t)) \cdot v(t) \\ \tau_{\text{drag}/r}(r(t)) \end{bmatrix}, \tag{19}$$

where $\tau_{\text{drag}/u}$, $\tau_{\text{drag}/v}$, and $\tau_{\text{drag}/r}$ represent the drag forces and moment in the x, y, and z directions, respectively. Polynomial functions in the x and y directions are determined by the velocity in the corresponding direction and heading angles. The polynomial function in the z direction is calculated by the yaw velocity. The specific formula for vector $\tau_{\text{drag}}(t)$ can be found in the previous work.

In the simulations, the generalized control inputs $\boldsymbol{\tau}_i$ computed by the MPC are applied directly to the TitoNeri model as body-fixed forces and moment. This corresponds to assuming that the azimuth thrusters can realize the requested surge, sway and yaw forces without significant allocation dynamics or saturation. Such an assumption is common in high-level motion control studies for small, fully actuated ASVs, where the thrust allocation module is treated as a separate low-level layer that distributes the desired generalized force vector to individual actuators [39–41]. In the present work, we therefore focus on the supervisory for-

Algorithm 1 Proposed centralized model predictive control algorithm

```
Require: Desired trajectory $y_i(t)$ and yaw $\psi_{ir}(t)$; Current position $y_{ic}(t)$, velocity
    $v_{is}(t)$, yaw angle $\psi_{ic}(t)$; Ship-to-ship interaction force $\tau_{is}(t)$
Ensure: Thruster input $\tau_i(k)$; ASV state $X_i(k)$
for $n = 1$ to $n_{\text{step}}$ do
    Discretize the desired trajectory from the top-level planner:
        $y_{iR}(k) = f(X_{iR}, U_{iR})$
    and pass it to the MPC controller
    Solve the optimization problem (see Eq. (18)) using current state and $y_{iR}(k)$
    to obtain $U_i(k)$
    Propagate the nonlinear 3-DOF plant model in simulation (e.g., using ode45)
    to obtain $\boldsymbol{X}_i(k+1)$.
    if target is reached then
        Break the loop
    end if
end for
```

Table 1 Parameters of the Tito-Neri

Parameters	Value	Parameters	Value
m	16.9	$Y_{\dot{v}}$	−49.2
I_z	$0.51L$	Y_r	0.0
x_g	0.0	$N_{\dot{v}}$	0.0
X_u	−1.2	N_r	−1.8

mation controller and do not explicitly model the thrust allocation algorithm or detailed thruster dynamics.

4.1 Platooning formation scenario

4.1.1 Setup

The objective is to cooperatively control three ASVs to navigate along their respective desired trajectories while maintaining the shape of the platooning formation under the influence of ship-to-ship interaction. In comparison with previous work, the desired trajectory consists of a straight segment followed by a circular trajectory. The parameters of this simulation are as shown in Table 5.

Where n represents the number of reference points, set as $n = 360$ and T represents the size of the simulation step per unit, set as $T = 1\,s$. The system constraints for ASV motion control are defined as follows:

$$\begin{bmatrix} -2 \\ -2 \\ -0.5 \end{bmatrix} \leq \tau_i \leq \begin{bmatrix} 2 \\ 2 \\ 0.5 \end{bmatrix}, \quad \begin{bmatrix} -2 \\ -2 \\ -0.5 \end{bmatrix} \leq \Delta\tau_i \leq \begin{bmatrix} 2 \\ 2 \\ 0.5 \end{bmatrix}. \quad (20)$$

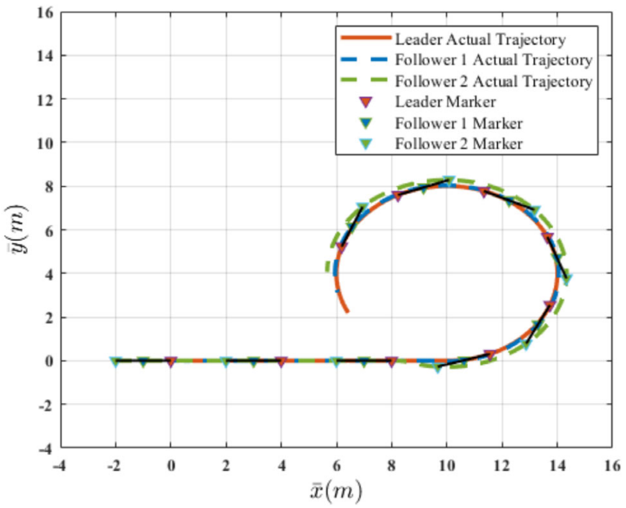

Fig. 3 The trajectories of three ASVs under platooning formation

4.1.2 Results and discussion

The results of platooning formation trajectory tracking are shown in Fig. 3. From $t = 0\,\text{s}$ to $t = 100\,\text{s}$, the formation moves along a straight line along the X-axis. Starting from $t = 100\,\text{s}$, the control objective changes to tracking a circle with a radius of 4 meters. Based on the inter-ship distances shown in Fig. 6, the leader ASV and the two follower ASVs are able to effectively track the desired trajectory while maintaining a platooning formation configuration. Moreover, when $t < 100$, the average error and maximum error during straight-line trajectory tracking are significantly smaller compared to those during circular trajectory tracking. This occurs because, during straight-line tracking, the lateral thrust and yaw moment are nearly zero, resulting in minimal disturbance to the ASV's motion. Consequently, only longitudinal forces from ship-to-ship interaction cause disturbances.

Figures 4 and 5 present the control inputs and velocity responses of the three ASVs across surge, sway, and yaw directions. As shown in Fig. 4, during the initial straight-line phase ($t < 100$ s), only surge thrust (τ_u) is applied, while lateral thrust and yaw moment remain close to zero. This indicates coordinated forward motion with minimal directional corrections. As the vessels transition into the circular trajectory, both lateral thrust (τ_v) and yaw moment (τ_r) start to fluctuate, reflecting the increased control effort required for turning and curvature adaptation. These inputs stabilize once each ASV settles into steady circular motion. Despite the transient fluctuations, all inputs remain within actuator limits and exhibit convergence behavior, demonstrating the controller's stability and constraint handling.

Figure 5 illustrates the evolution of the ASVs' velocities in all three degrees of freedom. The actual velocities closely track the reference commands throughout the maneuver. Velocity curves are smooth and well-damped, with particularly consistent yaw rates and lateral velocities during the circular path. Notably, the two follower vessels initiate lateral motion and yaw rotation slightly earlier than the leader to preserve formation geometry during the transition, which is evident in their earlier rise in v and r.

For better analysis and comparison, the following metric is used for evaluation: average surge velocity error rate $e_{iu} = \frac{1}{N}\sum_{n=1}^{N}\frac{|u_{it}-u_{iR}|}{|u_{iR}|}$. The results of the PID controller are taken from the work of [24], where the distance between ships is $1L$ and the speed is 0.1 m/s. The results are presented in Table 2.

The results demonstrate that the MPC controller surpasses the PID controller in both straight-line and circular trajectory tracking. In the platooning configuration, the leader ASV experiences the lowest overall error among the three vessels, aligning with the anticipated effects of ship-to-ship interaction. As illustrated in Fig. 7, the leader sustains the smallest longitudinal interaction force, which diminishes with decreasing speed. By contrast, the second follower exhibits the largest circular tracking error, mainly due to

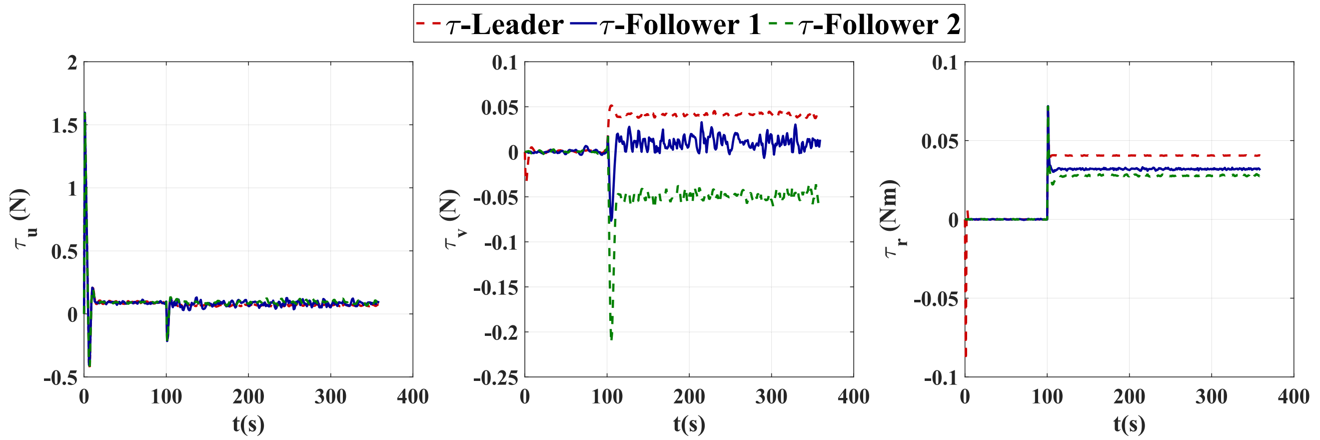

Fig. 4 Control input of three ASVs under platooning formation

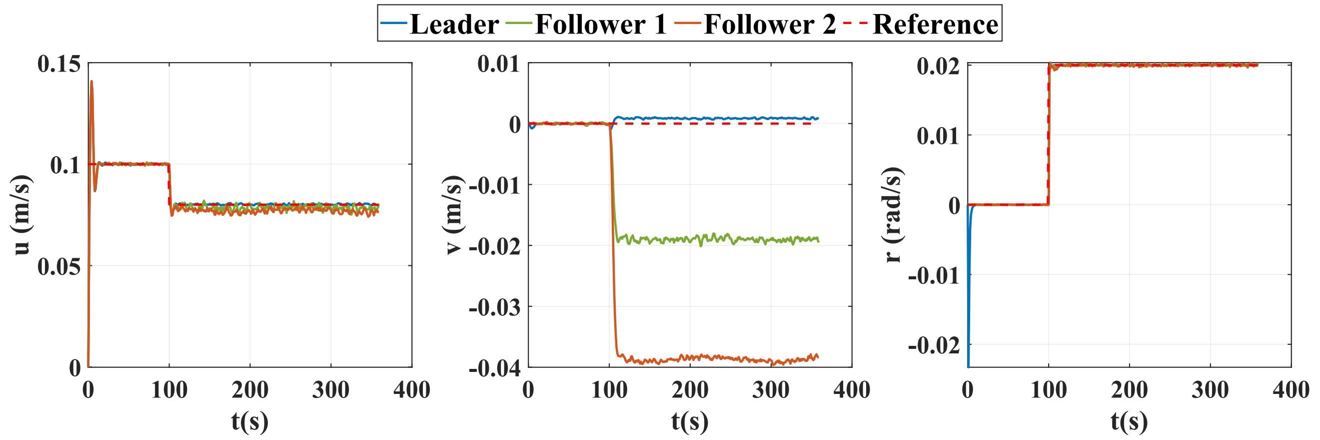

Fig. 5 Velocity of three ASVs under platooning formation

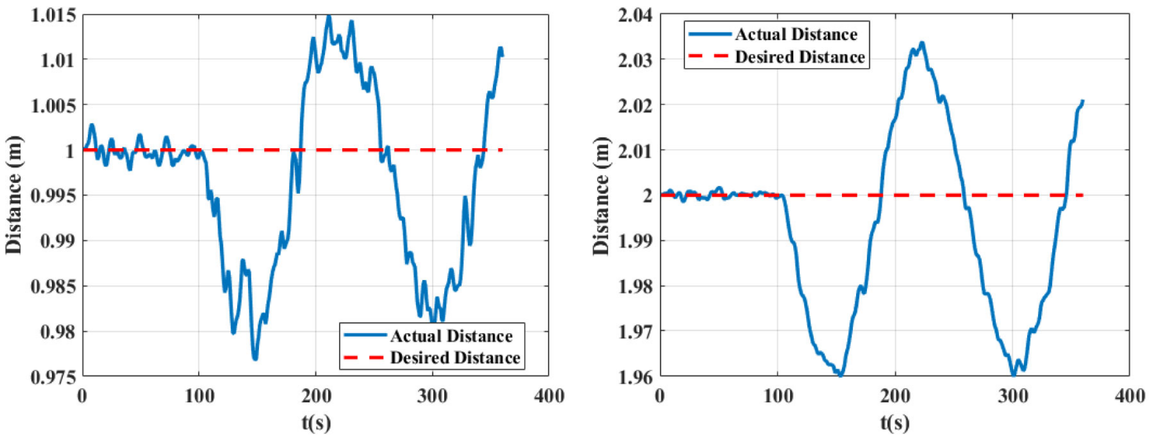

a b

Fig. 6 Distance in platooning formation: **a** The distances between the leader and follower-1 **b** The distances between the leader and follower-2

Table 2 Comparison of control performance between PID and MPC

Control method	e_u of PID	e_{iu} of MPC Leader ASV	Follower ASV$_1$	fFollower ASV$_2$
Straight-line trajectory	6.45%			
		3.31% ($n \leq 100$)	3.52% ($n \leq 100$)	3.32% ($n \leq 100$)
Circular trajectory				
		0.5% ($n > 100$)	2.1% ($n > 100$)	3.9% ($n > 100$)

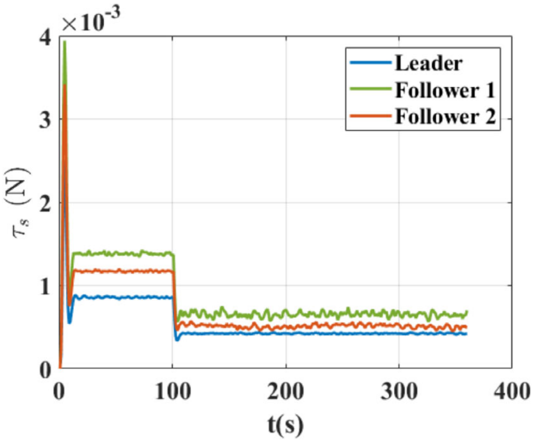

Fig. 7 Ship-to-ship interaction forces of three ASVs

its early anticipation upon entering the circular path. This is evident in Fig. 5, where, after 100 s, its sway velocity v undergoes the most pronounced fluctuation. Nevertheless, the overall errors remain within acceptable bounds.

The simulation results for the platooning formation demonstrate that the centralized MPC controller achieves superior trajectory tracking accuracy across all vessels. During curved maneuvers, the leader ASV is minimally affected by ship-to-ship interaction due to its frontmost position, while the trailing follower experiences the most pronounced disturbances. This spatial variation highlights the asymmetric propagation of hydrodynamic effects along the formation and underscores the controller's effectiveness in compensating for such interaction-induced deviations.

It should be noted that the PID benchmark in Table 2 corresponds only to the straight-line segment of the maneuver ($t < 100$ s). In our earlier study [24], even for a simpler two-vessel platooning scenario with straight-line motion, a conventional position-based PID controller already exhibited relatively large steady-state surge-velocity errors and oscillatory transients in the presence of ship-to-ship interaction. When the trajectory is extended with a circular segment and the scenario is generalized to the present three-vessel configuration, preliminary simulations show that the PID-controlled formation frequently develops large lateral and yaw excursions and, in some cases, fails to converge to the desired curved path. Reporting such non-convergent responses would not provide a meaningful quantitative benchmark and would be unfairly unfavorable to PID. Therefore, the comparison in Table 2 is deliberately restricted to the straight-line part of the platooning case, which represents the most benign operating condition for the PID controller and already highlights the performance improvement achieved by the proposed MPC scheme.

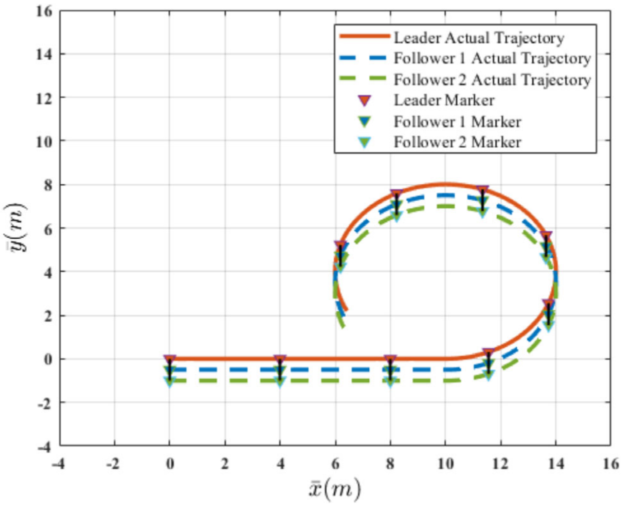

Fig. 8 The trajectories of three ASVs under parallel formation

Although the interaction forces are smaller than the commanded surge thrust in terms of absolute magnitude, their impact should be assessed through the induced state deviations over the mission time scale. Around an operating point, the linearised surge error dynamics can be expressed as

$$m_u\dot{\tilde{u}} = -d_u\tilde{u} + \tau_{is,u}, \tag{21}$$

which yields a steady-state speed bias $\tilde{u}_\infty = \tau_{is,u}/d_u$ and an accumulated position drift $\Delta x(t) = \int_0^t \tilde{u}(\sigma)\,d\sigma$. In close-spacing formations, $\tau_{is,u}$ acts as a persistent, geometry-dependent disturbance and may therefore lead to non-negligible spacing errors if not explicitly accounted for in the prediction model. For formation keeping, the relevant drift is the *relative* along-track error. Let $\tilde{S}_{ij}$ denote the longitudinal spacing error between vessels i and j. Then $\dot{\tilde{S}}_{ij} = \tilde{u}_i - \tilde{u}_j$, so even small differential biases in surge speed can accumulate into noticeable spacing errors over the mission horizon.

4.2 Parallel formation scenario

4.2.1 Setup

The objective of this simulation is to cooperatively control three ASVs to navigate along their respective desired trajectories while maintaining the shape of the parallel formation under the influence of ship-to-ship interaction. The parameters of this simulation are shown in Table 6.

4.2.2 Results and discussion

The simulation results for the parallel formation indicate that the centralized MPC controller maintains good tracking performance, comparable to that of the platooning case. However, the characteristics of the ship-to-ship interaction differ significantly. In platooning formations, the interactions predominantly occur along the longitudinal axis, whereas in parallel formations, the dominant effects appear in the lateral direction and yaw moment due to the side-by-side configuration.

As shown in Fig. 8, all three ASVs successfully follow the desired trajectory while preserving the parallel alignment. During the curved segment, the lateral thrust and yaw moment fluctuate more significantly than in the platooning case, as seen in Fig. 9. These oscillations are directly linked to the stronger sway and yaw disturbances, which in turn impact trajectory tracking. Although the lateral velocity v and yaw rate r are smaller in magnitude than the surge velocity u, their influence is more pronounced, especially in curved motion. This is evidenced by the dynamic spacing variations between vessels observed in Fig. 11.

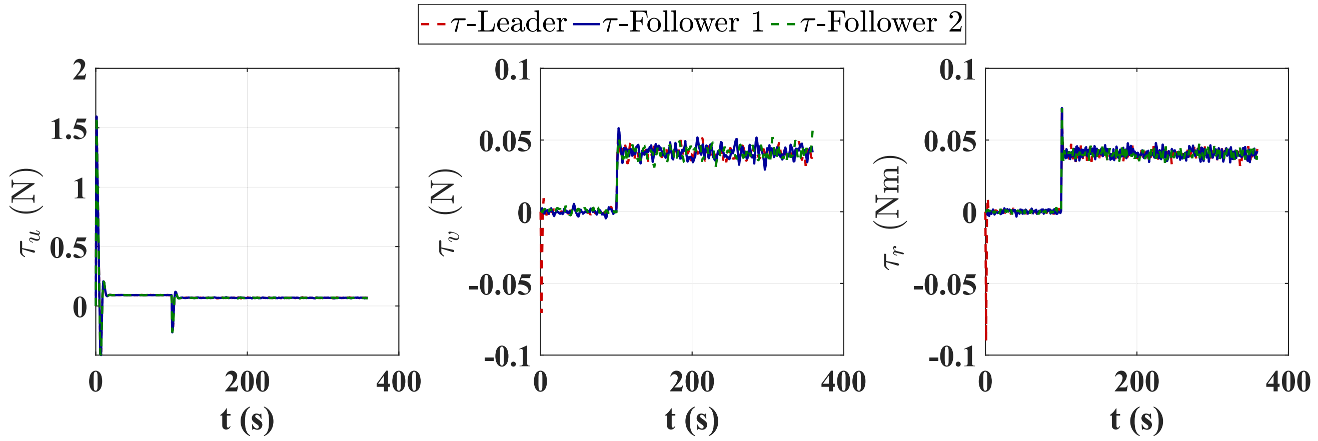

Fig. 9 Control input of three ASVs under parallel formation

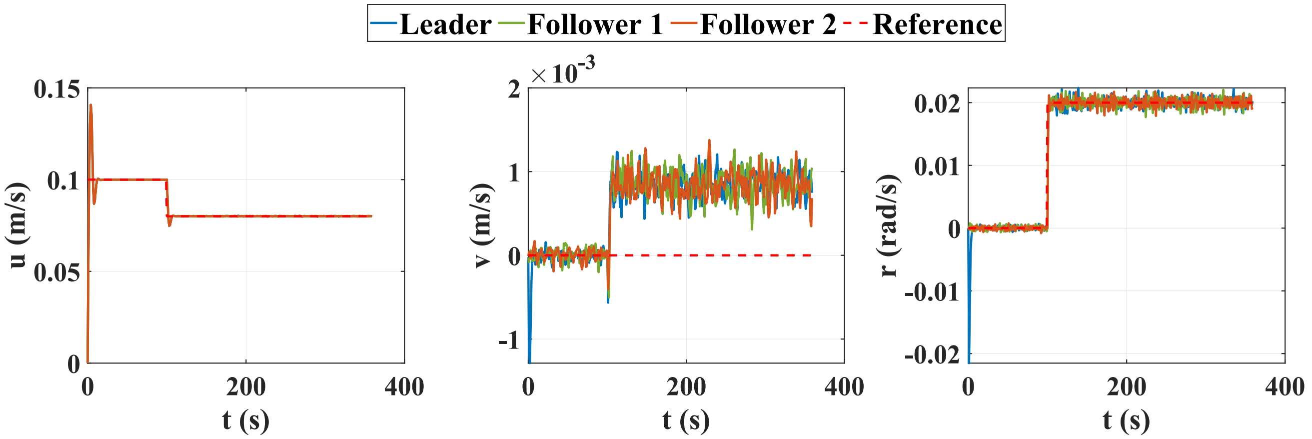

Fig. 10 Velocity of three ASVs under parallel formation

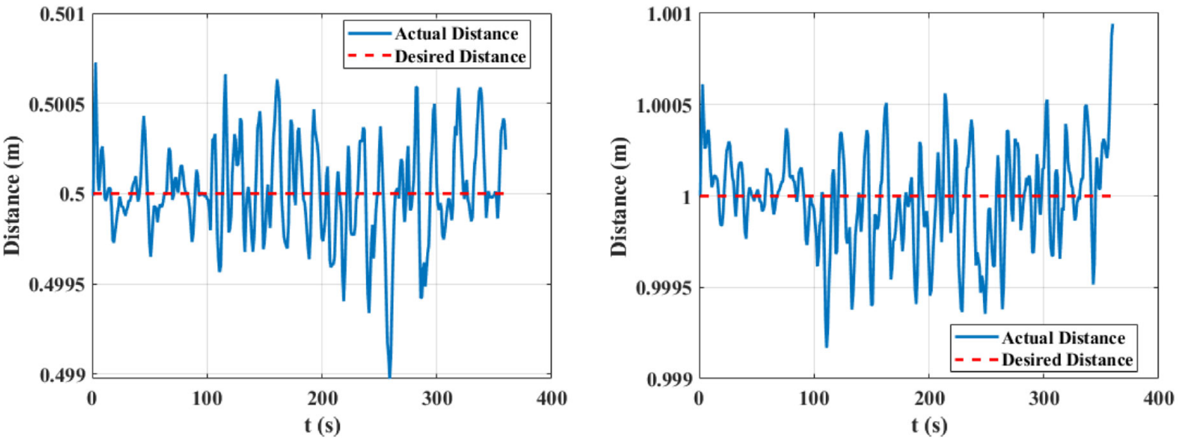

a Distance between the leader and follower-1

b Distance between the leader and follower-2

Fig. 11 Distance in parallel formation

Velocity tracking results in Fig. 10 reveal that, during straight-line motion, the surge velocity errors in parallel formation are nearly identical across all vessels, similar to the platooning case. However, in circular trajectories, a distinct reversal pattern is observed: the leader experiences greater surge velocity deviation than the followers. This contrasts with the platooning formation, where the leader typically exhibits the least deviation. The difference can be attributed to the fact that in parallel formation, the leader is more directly exposed to the compounded lateral flow field effects from the two follower ASVs, and its larger inertia makes it more sensitive to lateral-yaw coupling.

For better comparison with platooning formation, the trajectory is divided into straight-line and circular segments, using the following indicators: (1) Average surge velocity error rate $e_{iu} = \frac{1}{N}\sum_{n=1}^{N}\frac{|u_{it}-u_{iR}|}{|u_{iR}|}$; (2) Average sway velocity error $e_{iv} = \frac{1}{N}\sum_{n=1}^{N}|v_{it}-v_{iR}|$; 3) Average yaw error rate $e_{ir} = \frac{1}{N}\sum_{n=1}^{N}\frac{|r_{it}-r_{iR}|}{|r_{iR}|}$; 4) Average distance error rate $e_{iD} = \frac{1}{N}\sum_{n=1}^{N}\frac{|D_{it}-D_{iR}|}{|D_{iR}|}$. The results can be seen in Table 3.

According to the results in Table 3, during straight-line tracking, the parallel formation—despite being less influenced by longitudinal hydrodynamic interactions—achieves a surge velocity error (e_{iu}) comparable to that of the platooning formation. All three ASVs in the parallel case exhibit nearly identical surge errors (approximately 3.08%), similar to the tightly grouped errors seen in the platooning case (3.31–-3.52%). However, in the circular trajectory, a clear reversal trend emerges. In the parallel formation, the leader exhibits the largest surge velocity error ($e_{iu} = 3.27\%$), while the two followers achieve notably lower values ($e_{iu} = 3.04\%, 3.08\%$). This contrasts with the platooning formation, where the leader's error is the smallest (0.5%) and the followers experience slightly higher deviations. From

Table 3 Comparison of control performance across different configurations

Formation configuration	ASV	Straight-line trajectory				Circular trajectory			
		e_{iu} (%)	e_{iv}	e_{ir}	e_{iD}	e_{iu} (%)	e_{iv}	e_{ir} (%)	e_{iD} (%)
Platooning	Leader	3.31	–	–	–	0.5	0.001	0.5	–
	Follower$_1$	3.52	–	–	0.08	2.1	0.019	0.8	1.04
	Follower$_2$	3.32	–	–	0.02	3.9	0.038	0.9	1.08
Parallel	Leader	3.08	8.2e−5	5.9e−4	–	3.27	8.4e−4	3.45	–
	Follower$_1$	3.07	5.8e−5	2.8e−4	0.02	0.31	8.5e−4	3.58	0.05
	Follower$_2$	3.08	5.3e−5	2.4e−4	0.01	0.32	8.3e−4	3.34	0.02

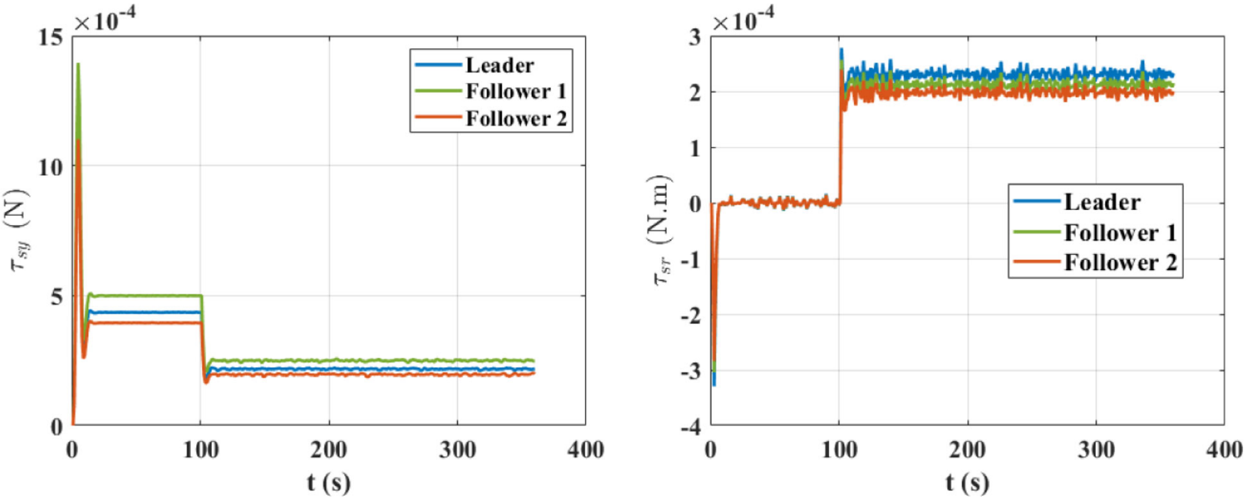

a Lateral forces τ_{sy}

b moments τ_{sr}

Fig. 12 Ship-to-ship interaction forces and moments under parallel formation

a control perspective, this distinction stems from the spatial interaction structure. In parallel formation, the leader is directly exposed to the lateral flow disturbances generated by the followers, and its higher mass inertia makes it more sensitive to perturbations in sway velocity and yaw rate. As a result, even small variations in v and r can propagate into larger surge deviations, especially under curved path conditions.

The corresponding interaction-force profiles in Fig. 12 further clarify this mechanism. In the parallel configuration the vessels sailing abreast experience markedly larger sway forces and yaw moments than in the platooning case, with opposite signs for the leader and the followers. These geometry-induced disturbances correlate directly with the spacing variations in Fig. 11 and the surge-velocity reversals observed in Fig. 10, confirming that the lateral and yaw components of the interaction model are essential for explaining the different formation behaviors.

4.3 Triangular formation scenario

4.3.1 Setup

The objective of this simulation is to cooperatively control three ASVs to navigate along their respective desired trajectories while maintaining the shape of the triangular formation under the influence of ship-to-ship interaction. The parameters of this simulation are shown in Table 7. In the table, $\theta_1 = 2/3\pi, \theta_2 = -2/3\pi$.

4.3.2 Results and discussion

The triangular formation exhibits tracking behavior comparable to the platooning and parallel configurations, but introduces more balanced ship-to-ship interaction across all three degrees of freedom. As shown in Fig. 13, the proposed control strategy successfully maintains formation geometry and tracks the reference trajectory, even under combined surge, sway, and yaw disturbances.

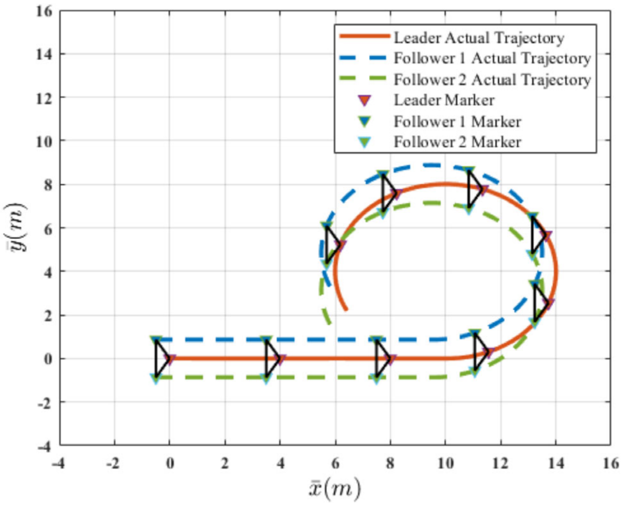

Fig. 13 The trajectories of three ASVs under triangular formation

Compared to the other formations, the triangular setup experiences moderate oscillations in all control channels (Fig. 14), with no single DOF dominating the interaction forces. This is further reflected in the velocity profiles (Fig. 15), where all three vessels exhibit smooth, well-damped responses. Notably, lateral and yaw fluctuations are smaller than those in parallel formation, while surge control remains as stable as in the platooning case.

Inter-ship spacing remains consistent throughout the maneuver (Fig. 16), highlighting the controller's ability to maintain formation cohesion. Although interaction forces are present in all DOFs (Fig. 17), their magnitudes are relatively smaller than in the other two configurations, reducing their impact on control effort and contributing to improved performance.

According to Tables 3 and 4, during straight-line tracking, the triangular formation achieves surge velocity errors (e_{iu}) between 3.11% and 3.14%, which are slightly lower than those observed in the platooning formation (3.31-–3.52%) and similar to the parallel case. This suggests that, despite multi-axis interactions, the triangular formation maintains a stable surge response. Since lateral velocity v and yaw rate r are near zero during this phase, control effort is focused

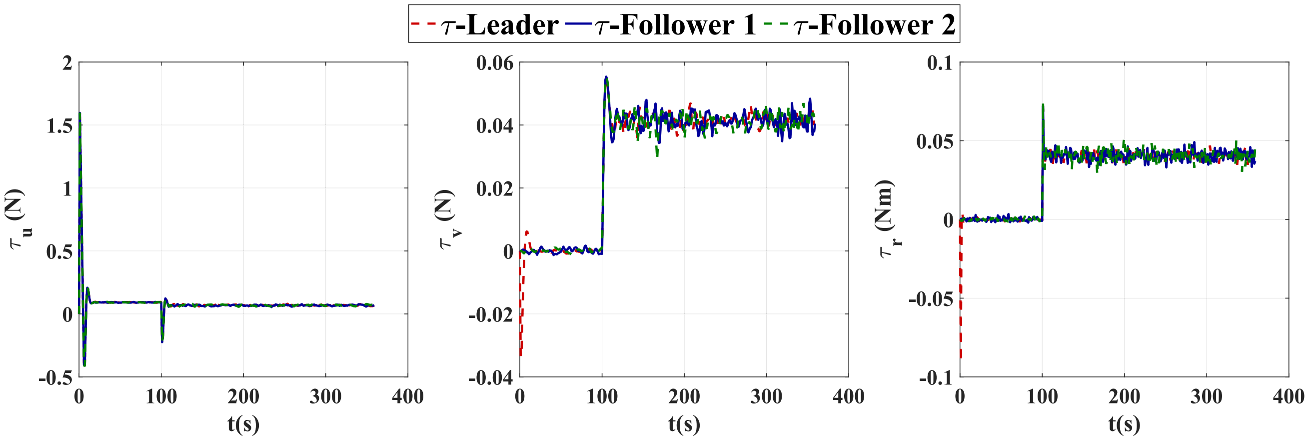

Fig. 14 Control input of three ASVs under triangular formation

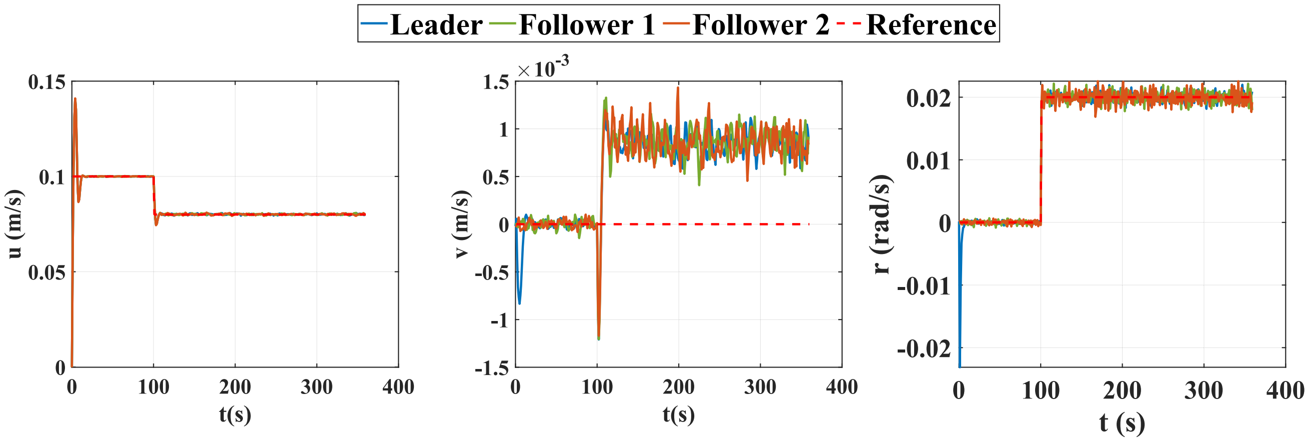

Fig. 15 Velocity of three ASVs under triangular formation

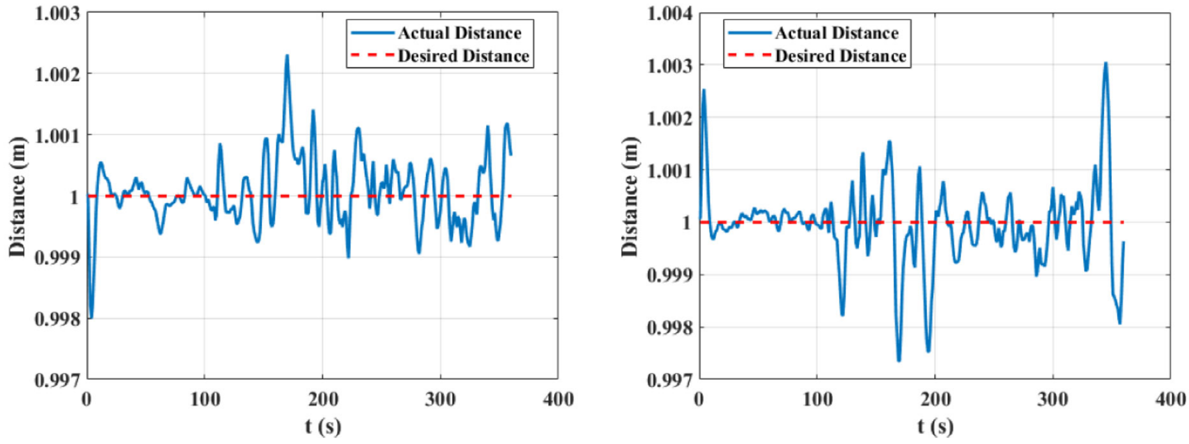

a Distance between the leader and follower-1

b Distance between the leader and follower-2

Fig. 16 Distance in triangular formation

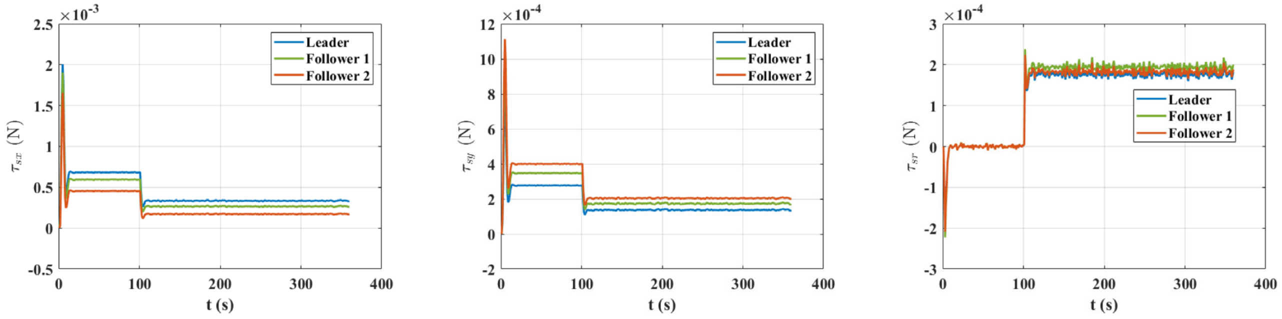

a Longitudinal forces τ_{sx}

b Lateral forces τ_{sy}

c yaw moments τ_{sr}

Fig. 17 Ship-to-ship interaction forces and moments under triangular formation

primarily on surge direction, although residual sway or yaw effects may still propagate into surge error.

During circular motion, the triangular formation achieves the best overall performance, with surge velocity errors reduced to around 0.5% for all vessels. In contrast, both platooning and parallel configurations exhibit surge errors above 3%. Moreover, the triangular formation maintains balanced tracking in lateral and yaw dynamics—outperforming platooning (which neglects lateral/yaw interactions) and closely matching the stability achieved in the parallel configuration. These results demonstrate the triangular formation's robustness and control effectiveness under full-axis interaction conditions.

Table 4 Comparison of control performance across different configurations

Formation configuration	ASV	Straight-line trajectory				Circular trajectory			
		e_{iu} (%)	e_{iv}	e_{ir}	e_{iD} (%)	e_{iu} (%)	e_{iv}	e_{ir} (%)	e_{iD} (%)
Platooning	Leader	3.31	–	–	–	0.5	0.001	0.5	–
	Follower$_1$	3.52	–	–	0.08	2.1	0.019	0.8	1.04
	Follower$_2$	3.32	–	–	0.02	3.9	0.038	0.9	1.08
triangular	Leader	3.12	7.2e−05	5.4e−04	–	0.496	8.4e−04	2.96	–
	Follower$_1$	3.11	3.74e−05	2.2e−04	0.024	0.494	8.7e−04	3.91	0.047
	Follower$_2$	3.14	3.0e−05	2.3e−04	0.022	0.547	8.5e−04	4.34	0.061

5 Conclusions and future research

This study proposed a centralized MPC framework for multi-vessel formation control that explicitly accounts for ship-to-ship interaction effects using a data-informed, three-degree-of-freedom empirical model. Unlike conventional approaches that ignore hydrodynamic coupling or rely on oversimplified formulations, the interaction model in this work is constructed and calibrated from existing CFD datasets, enabling efficient estimation of proximity-induced forces without resorting to first-principles derivation. To improve lateral stability and tracking smoothness, particularly in curved trajectories, a coordinate transformation was introduced in the controller design to decouple yaw-induced sway motion. The overall framework thus integrates trajectory tracking and disturbance adaptation in a unified setting and is validated through simulations across three representative formation patterns: platooning, parallel, and triangular.

Simulation results confirm that the empirical interaction model, though compact, effectively approximates the surge, sway, and yaw disturbances caused by neighboring vessels in close-range operations. The proposed MPC controller outperforms a conventional PID benchmark in terms of formation stability and tracking accuracy in the straight-line platooning scenario, where PID remains marginally functional, and maintains bounded, well-damped responses on curved trajectories and for all three formation geometries. Formation-specific behaviors are observed: the platooning formation exhibits superior stability in curved paths, the parallel formation is more prone to lateral deviation due to asymmetric interactions, and the triangular formation provides relatively balanced performance across all vessels. These findings highlight the practicality of the proposed approach in capturing key dynamic effects and ensuring robust formation control under proximity-induced disturbances.

This work focuses on interaction-aware formation MPC under a 3-DOF manoeuvring model and neglects environmental disturbances. Future work will (i) incorporate wind, current and wave loads and actuator allocation where relevant, and (ii) extend validation to higher-fidelity models (e.g., 6-DOF) and experimental platforms.

Appendix A: Additional simulation parameters

See Tables 5, 6 and 7.

Table 5 Parameters of the platooning formation control simulation

Physical	Leader ASV	Follower ASV$_1$	Follower ASV$_2$
p_i	$x_R = 0.1n,\ n < 100$ $x_R = 10 + 4\sin(0.02(n-100))$ $y_R = 0,\ n < 100$ $y_R = 4(1-\cos(0.02(n-100)))$	$x_{R_2} = x_R - 1,\ n < 100$ $x_{R_2} = x_R - \cos(0.02(n-100))$ $y_{R_2} = y_R,\ n < 100$ $y_{R_2} = y_R - \sin(0.02(n-100))$	$x_{R_3} = x_R - 2,\ n < 100$ $x_{R_3} = x_R - 2\cos(0.02(n-100))$ $y_{R_3} = y_R,\ n < 100$ $y_{R_3} = y_R - 2\sin(0.02(n-100))$
$X_i(0)$	(0, 0, 0.04, 0, 0, 0)	(-1, 0, 0, 0, 0, 0)	(-2, 0, 0, 0, 0, 0)
N_p, N_c	10, 8	10, 8	10, 8
Q_i, R_i	$\begin{bmatrix} 10 & 0 & 0 \\ 0 & 1 & 0 \\ 0 & 0 & 10 \end{bmatrix}, \begin{bmatrix} 1 & 0 & 0 \\ 0 & 1 & 0 \\ 0 & 0 & 1 \end{bmatrix}$	Same as left	Same as left
α	$\begin{bmatrix} 0.99 & -0.013 & 0 \\ 0 & 0 & 0 \\ 0 & 0 & 0 \end{bmatrix}$	$\begin{bmatrix} 1.51 & -0.014 & 0 \\ 0 & 0 & 0 \\ 0 & 0 & 0 \end{bmatrix}$	$\begin{bmatrix} 1.34 & -0.017 & 0 \\ 0 & 0 & 0 \\ 0 & 0 & 0 \end{bmatrix}$

Table 6 Parameters of the Parallel formation control simulation

Physical	Leader ASV	Follower ASV$_1$	Follower ASV$_2$
p_i	$x_R = 0.1n,\ n < 100$ $x_R = 10 + 4\sin(0.02(n - 100))$	$x_{R_2} = x_R$	$x_{R_3} = x_R$
	$y_R = 0,\ n < 100$ $y_R = 4(1 - \cos(0.02(n - 100)))$	$y_{R_2} = y_R - 0.5$	$y_{R_3} = y_R - 1$
$X_i(0)$	(0, 0, 0.04, 0, 0, 0)	(0, −0.5, 0, 0, 0, 0)	(0, -1, 0, 0, 0, 0)
N_p, N_c	10, 8	10, 8	10, 8
Q_i, R_i	$\begin{bmatrix} 1 & 0 & 0 \\ 0 & 10 & 0 \\ 0 & 0 & 10 \end{bmatrix}, \begin{bmatrix} 1 & 0 & 0 \\ 0 & 1 & 0 \\ 0 & 0 & 1 \end{bmatrix}$	Same as left	Same as left
α	$\begin{bmatrix} 0 & 0 & 0 \\ 0.43 & 0 & -7.46 \\ 22.5 & 0 & -3.1 \end{bmatrix}$	$\begin{bmatrix} 0 & 0 & 0 \\ 0.49 & 0 & -8.75 \\ 19.4 & 0 & -2.2 \end{bmatrix}$	$\begin{bmatrix} 0 & 0 & 0 \\ 0.39 & 0 & -7.28 \\ 17.5 & 0 & -2.8 \end{bmatrix}$

Table 7 Parameters of the triangular formation control simulation

Physical	Leader ASV	Follower ASV$_1$	Follower ASV$_2$
$p_i(x)$	$x_R = 0.1n,\ n < 100$ $x_R = 10 + 4\sin(0.02(n - 100))$	$x_{R_2} = x_R + \cos(\theta_1)$	$x_{R_3} = x_R + \cos(\theta_2)$
$p_i(y)$	$y_R = 0,\ n < 100$ $y_R = 4(1 - \cos(0.02(n - 100)))$	$y_{R_2} = y_R + \sin(\theta_1)$	$y_{R_3} = y_R + \sin(\theta_2)$
$X_i(0)$	(0, 0, 0.04, 0, 0, 0)	(−0.5, 0.87, 0, 0, 0, 0)	(−0.5, −0.87, 0, 0, 0, 0)
N_p, N_c	10, 8	10, 8	10, 8
Q_i, R_i	$\begin{bmatrix} 10 & 0 & 0 \\ 0 & 10 & 0 \\ 0 & 0 & 10 \end{bmatrix}, \begin{bmatrix} 1 & 0 & 0 \\ 0 & 1 & 0 \\ 0 & 0 & 1 \end{bmatrix}$	$\begin{bmatrix} 10 & 0 & 0 \\ 0 & 10 & 0 \\ 0 & 0 & 10 \end{bmatrix}, \begin{bmatrix} 10 & 0 & 0 \\ 0 & 1 & 0 \\ 0 & 0 & 1 \end{bmatrix}$	$\begin{bmatrix} 1 & 0 & 0 \\ 0 & 10 & 0 \\ 0 & 0 & 10 \end{bmatrix}, \begin{bmatrix} 1 & 0 & 0 \\ 0 & 1 & 0 \\ 0 & 0 & 1 \end{bmatrix}$
α	$\begin{bmatrix} 0.81 & -0.033 & 0.008 \\ 0.28 & 1.1 & -12.1 \\ 17.3 & -0.84 & -2.1 \end{bmatrix}$	$\begin{bmatrix} 0.91 & -0.037 & -0.005 \\ 0.35 & -2.4 & -7.25 \\ 19.1 & -0.55 & -2.2 \end{bmatrix}$	$\begin{bmatrix} 0.94 & -0.037 & -0.011 \\ 0.4 & -0.62 & -2.21 \\ 17.9 & -1.1 & -2.8 \end{bmatrix}$

Acknowledgements This research is supported by the Researchlab Autonomous Shipping (RAS) of Delft University of Technology.

Author Contributions Xin Xiong: Conceptualization, methodology, software, investigation, writing—original draft, visualization. Rudy R. Negenborn: Conceptualization, writing—review and editing, supervision, project administration. Yusong Pang: Conceptualization, methodology, writing—review and editing, supervision, project administration.

Data availability This study is based on numerical simulations. The data supporting the findings of this study are available from the authors upon reasonable request.

References

1. Makar A (2022) Determination of the minimum safe distance between a USV and a hydro-engineering structure in a restricted water region sounding. Energies 15(7):2441
2. Qiao Y, Yin J, Wang W, Duarte F, Yang J, Ratti C (2023) Survey of deep learning for autonomous surface vehicles in marine environments. IEEE Trans Intell Transp Syst 24(4):3678–3701
3. Gao K, Gao M, Zhou M, Ma Z (2024) Artificial intelligence algorithms in unmanned surface vessel task assignment and path planning: a survey. Swarm Evol Comput 86:101505
4. Zhao C, Thies PR, Johanning L (2022) Offshore inspection mission modelling for an ASV/ROV system. Ocean Eng 259:111899
5. Negenborn RR, Goerlandt F, Johansen TA, Slaets P, Valdez Banda OA, Vanelslander T, Ventikos NP (2023) Autonomous ships are on the horizon: here's what we need to know. Nature 615(7950):30–33
6. Chen L, Negenborn RR, Huang Y, Hopman H (2020) Survey on cooperative control for waterborne transport. IEEE Intell Trans Syst Mag 13(2):71–90
7. Liu L, Wang D, Peng Z, Li T (2017) Modular adaptive control for LOS-based cooperative path maneuvering of multiple underactuated autonomous surface vehicles. IEEE Trans Syst Man Cybern Syst 47(7):1613–1624
8. Liu Y, Bucknall R (2015) Path planning algorithm for unmanned surface vehicle formations in a practical maritime environment. Ocean Eng 97:126–144
9. Gu N, Wang D, Peng Z, Liu L (2020) Adaptive bounded neural network control for coordinated path-following of networked

underactuated autonomous surface vehicles under time-varying state-dependent cyber-attack. ISA Trans 104:212–221

10. Dai S-L, He S, Chen X, Jin X (2019) Adaptive leader-follower formation control of nonholonomic mobile robots with prescribed transient and steady-state performance. IEEE Trans Industr Inf 16(6):3662–3671
11. Zhang G, Yu W, Zhang W, Huang C (2022) Robust adaptive formation control of underactuated surface vehicles with the desired-heading amendment. J Mar Sci Technol 27(1):138–150
12. Wang H, Luo Q, Li N, Zheng W (2022) Data-driven model free formation control for multi-USV system in complex marine environments. Int J Control Autom Syst 20(11):3666–3677
13. Tan G, Zhuang J, Zou J, Wan L (2023) Adaptive adjustable fast marching square method based path planning for the swarm of heterogeneous unmanned surface vehicles (usvs). Ocean Eng 268:113432
14. Qin D, Liu A, Zhang D, Ni H (2020) Formation control of mobile robot systems incorporating primal-dual neural network and distributed predictive approach. J Franklin Inst 357(17):12454–12472
15. Fahimi F (2007) Sliding-mode formation control for underactuated surface vessels. IEEE Trans Rob 23(3):617–622
16. He S, Wang M, Dai S-L, Luo F (2018) Leader-follower formation control of USVs with prescribed performance and collision avoidance. IEEE Trans Ind Inf 15(1):572–581
17. Dong Z, Zhang Z, Qi S, Zhang H, Li J, Liu Y (2023) Autonomous cooperative formation control of underactuated USVs based on improved MPC in complex ocean environment. Ocean Eng 270:113633
18. Jiang X, Peng M, Li Z, Huang L, Xu S, Yang K-J (2023) Robust multistage nonlinear model predictive control on an autonomous marine surface vehicle. J Mar Sci Technol 28(2):370–386
19. Zhou X, Wu Y, Huang J (2020) MPC-based path tracking control method for USV. In: 2020 Chinese automation congress (CAC), pp 1669–1673. IEEE
20. Zhu Y, Li S, Guo G, Yuan P, Bai J (2024) Formation control of UAV-USV based on distributed event-triggered adaptive MPC with virtual trajectory restriction. Ocean Eng 294:116850
21. Wen G, Lam J, Fu J, Wang S (2023) Distributed MPC-based robust collision avoidance formation navigation of constrained multiple USVs. IEEE Trans Intell Veh
22. Tang Z, Wang L, Wang Y, He H, Li B (2022) Distributed-integrated model predictive control for cooperative operation with multi-vessel systems. J Mar Sci Technol 27(4):1281–1301
23. He Y, Mou J, Chen L, Zeng Q, Chen P, Zhang S (2021) Survey on hydrodynamic effects on cooperative control of maritime autonomous surface ships. Ocean Eng 235:109300
24. Xiong X, Negenborn RR, Pang Y (2024) Influence of ship-to-ship interaction on formation control of multi-vessel systems. In: Proceedings of the 21st international conference on informatics in control, automation and robotics, Vol 1, pp 25–36
25. Koop A (2020) Using CFD to determine scale effects on current loads of offshore vessels in side-by-side configuration. Ocean Eng 195:106707
26. Dong Z, Liang X, Guan X, Li W (2022) Formation optimization of various spacing configurations for a fleet of unmanned surface vehicles based on a hydrodynamic energy-saving strategy. Ocean Eng 266:112824
27. He Y, Mou J, Chen L, Zeng Q, Huang Y, Chen P, Zhang S (2022) Will sailing in formation reduce energy consumption? Numerical prediction of resistance for ships in different formation configurations. Appl Energy 312:118695
28. Fossen TI (2011) Handbook of Marine craft hydrodynamics and motion control. Wiley, Chichester
29. Vantorre M, Verzhbitskaya E, Laforce E (2002) Model test based formulations of ship-ship interaction forces. Ship Technol Res 49:124–141
30. Yu D, Wang L, Yeung RW (2019) Experimental and numerical study of ship-to-ship interactions in overtaking manoeuvres. Proceed R Soc A 475(2225):20180748
31. Yuan Z-M, Kellet P, Incecik A, Turan O, Boulougouris E (2015) Ship-to-ship interaction during overtaking operation in shallow water. J Ship Res 59(03):172–187
32. De Decker B (2006) Ship-ship interaction during lightering operations. maritime technology division, ghent university. PhD thesis, M. Sc. Dissertation
33. Lataire E, Vantorre M, Delefortrie G, Candries M (2012) Mathematical modelling of forces acting on ships during lightering operations. Ocean Eng 55:101–115
34. Setiawan H, Muin M (2018) Dynamic response of breasting dolphin moored with 40,000 dwt ship due to parallel passing ship phenomenon. In: MATEC web of conferences, vol 147, p 05003. EDP Sciences
35. Du Z, Reppa V, Negenborn RR (2021) Mpc-based colregs compliant collision avoidance for a multi-vessel ship-towing system. In: 2021 European control conference (ECC), pp 1857–1862 . IEEE
36. Do KD (2011) Practical formation control of multiple underactuated ships with limited sensing ranges. Robot Auton Syst 59(6):457–471
37. Satoh T, Kaneko K, Saito N (2012) Improving tracking performance of predictive functional control using disturbance observer and its application to table drive systems. Int J Comput Commun Control 7(3):550–564
38. Haseltalab A, Negenborn RR (2019) Model predictive maneuvering control and energy management for all-electric autonomous ships. Appl Energy 251:113308
39. Fossen TI, Johansen TA (2006) A survey of control allocation methods for ships and underwater vehicles. In: 2006 14th Mediterranean conference on control and automation, pp 1–6
40. Liu C, Negenborn RR, Chu X, Zheng H (2018) Predictive path following based on adaptive line-of-sight for underactuated autonomous surface vessels. J Mar Sci Technol 23(3):483–494
41. Li Z, Li R, Bu R (2021) Path following of under-actuated ships based on model predictive control with state observer. J Mar Sci Technol 26(2):408–418